Demonstration of Large Curvature Radius Shape Sensing Using Optical Frequency Domain Reflectometry in Multi-Core Fibers

Zeen Chen, Chenhuan Wang, Zhenyang Ding, Dongfang Zhu, Haohan Guo, Ming Pan, Yin Yu, Kun Liu, Junfeng Jiang, and Tiegen Liu

***Abstract*—In distributed shape sensing, the shape reconstruction error is more and more sensitive to the strain measuring error along with curvature radius of reconstructed shape increasing, which causes a notable challenge for large curvature radius shape reconstructing. In this paper, we demonstrate a large curvature radius shape sensing using optical frequency domain reflectometry (OFDR) in multi-core fibers. We construct a theoretical model of strain measuring error and curvature radius reconstructing errors under different curvature radius. In the experiment, by this reconstructing error model, we optimally select the measurable strain resolution and the sensing spatial resolution to realize the shape reconstruction with a large curvature radius and reconstruct two-dimensional (2D) circle shapes of curvature radii from 5 cm to 100 cm. To verify the accuracy of three-dimensional (3D) shape reconstruction, we present a 3D shape sensing validation method based on 3D printing technology. We fabricate a 3D phantom containing a groove with a variable curvature radius of 5 cm to 100 cm. The presented distributed shape sensing system realize to reconstruct this complicated 3D shape. The root-mean-square error of curvature radius between the reconstructed and designed 3D space curves is 7.2 mm and the mean Euclidean distance is 3.4 mm.**

***Index Terms*—Optical sensors, optical fiber sensors, distributed optical fiber sensing, optical frequency domain reflectometry, shape sensing.**

Manuscript received May 3, 2021; revised July 12, 2021; accepted July 15, 2021. Date of publication July 21, 2021; date of current version August 5, 2021. This work was supported in part by the National Natural Science Foundation of China (NSFC) under Grants 61975147, 61635008, 61735011, and 61505138, in part by the National Key Research and Development Program under Grant 2019YFC0120701, in part by the Special Technical Support Project of China Market Supervision and Administration under Grant 2021YJ027, in part by the Tianjin Science and Technology Support Plan Program Funding under Grant 16JCQNJC01800, in part by China Postdoctoral Science Foundation under Grants 2015M580199 and 2016T90205, and in part by National Instrumentation Program under Grant 2013YQ030915. *(Zeen Chen and Chenhuan Wang contributed equally to this work.) (Corresponding author: Zhenyang Ding.)*

Zeen Chen, Chenhuan Wang, Zhenyang Ding, Haohan Guo, Ming Pan, Yin Yu, Kun Liu, Junfeng Jiang, and Tiegen Liu are with the School of Precision Instruments and Opto-Electronics Engineering, Tianjin University, Tianjin 300072, China, with Tianjin Optical Fiber Sensing Engineering Center, Institute of Optical Fiber Sensing of Tianjin University, Tianjin 300072, China, and also with Key Laboratory of Opto-electronics Information Technology, Tianjin University, Ministry of Education, Tianjin 300072, China (e-mail: 907828093@qq.com; wang_chen_huan@163.com; zyding@tju.edu.cn; 1186694962@qq.com; ming_pan@tju.edu.cn; nankai69@163.com; beiyangkl@tju.edu.cn; jiangjfjxu@tju.edu.cn; tgliu@tju.edu.cn).

Dongfang Zhu is with the Shanghai Aerospace Control Technology Institute, Shanghai 201109, China (e-mail: dongfang0704@126.com).

Digital Object Identifier 10.1109/JPHOT.2021.3098300

I. Introduction

DISTRIBUTED shape sensing (DSS) is becoming a hot area of distributed optical fiber sensing [1], which has been applied to fields such as medical robotics [2], industrial robotics [3], aerospace [4], [5], mining industry [6], [7] and so on. Distributed and quasi-distributed optical fiber sensing (DOFS and QDOFS) can achieve directional strain measurements. A DOFS or QDOFS can use a tri-core sensing fiber to measure strain on each core, which is consequently used in a differential geometry model to reconstruct the three-dimensional (3D) shape of the sensing fiber.

Fiber Bragg grating (FBG) as a QDOFS technology was firstly used to 3D distributed shape sensing [8]. However, the arrangement density of FBGs is limited, resulting a low accuracy of 3D shape reconstructing. DOFS use an entire optical fiber as sensing media that is an ideal technology for 3D distributed shape sensing. Zhao *et al.* used a Brillouin optical time domain analysis (BOTDA) technique to realize DSS with a sensing range of 1 km. However, the spatial resolution of this system is only 20 cm [9]. Szostkiewicz *et al.* used a phase-sensitive optical time-domain reflectometry (phase-OTDR) to achieve DSS. Although the strain sensing sensitivity of phase-OTDR is up to nano-strain level, the spatial resolution of this system is still not high, about 10 cm [10]. In addition, the static strain measurement using phase-OTDR is not very stable because the phase is easily influenced by extern environment vibration. Above all, the strain sensing spatial resolution of FBGs and DOFS based on time domain techniques are not very high, which will influence the accuracy of DSS.

Optical frequency domain reflectometry (OFDR) is an ideal approach to realize a distributed strain sensing with high spatial resolution and high sensitivity simultaneously. Froggatt *et al.* proposed a distributed strain and temperature sensing based on the optical frequency shifts of Rayleigh backscattering spectra (RBS). The minimal measurable strain is up to 1 $\mu\varepsilon$ [11], [12] and the sensing spatial resolution is up to 1 cm. OFDR is very suitable for DSS. Duncan *et al.* firstly applied OFDR to DSS [13], which has been contributed in the advancement of the "da Vinci Surgical System" [1]. Parent *et al.* used UV exposed fibers to enhanced the accuracy of shape reconstruction in OFDR [2] and they have developed this technology to achieve an advanced interventional guidance platform [14]. Shao *et al.* presented a

local spectrum matching method for OFDR based DSS [15]. Zhao *et al.* presented a dual-parameter sensor that can simultaneously measure the shape and temperature in OFDR [16]. Yin *et al.* presented a distributed directional torsion sensing in OFDR [17]. The reconstructing error of DSS is closely related to maximal curvature radius of reconstructed shape, but this issues is usually neglected in the previous methods. However, previous researches focus on shape reconstruction with small curvature radius of several centimeters [3], [14], [16], [18], [19]. For example, the reconstructing curvature radius is less than 1 mm in [14], from 5 cm to 30 cm in [16], 5 cm in [18]. Researches about curvature radius of several ten centimeters to several meters shape reconstruction is very limited. A shape reconstructing with large curvature radius of more than 1 m is a notable challenge, because it requires a tiny strain measurement error of less than 1 micro-strain. A theoretical model of strain measuring error and reconstructing errors is necessary to guide strain measurement in DSS, which is significant for large curvature radius shape reconstructing. In addition, the research of shape reconstruction error only focuses on Euclidean distance deviation between the reconstructed and designed shape [13]. However, the curvature or curvature radius reconstructing error is also key assessment criteria for the shape reconstruction error, which research is also limited.

Traditional verification methods of shape sensing are usually based on 2D plane curve such as a plane curve on a graph paper [9], [20]. When 3D shape sensing is used to verify 3D space curve, the accurate space positions of 3D space curve is difficult to be acquired [18], [21]. 3D phantom fabricated by computer numerical control (CNC) milling machine [14], [19] is used to verify 3D shape sensing, but this phantom cannot provide curvature radius information directly and extra registration process is necessary. Imaging methods such as photogrammetry system [22], magnetic resonance imaging (MRI) [23] computed tomography (CT) scan [24] were used to gain the actual 3D coordinates position of the sensing fiber, but imaging methods belong to indirect verification, whose accuracy is influenced by imaging resolution and quality. In addition, these imaging systems are high cost and not available for common labs. 3D printing is a rapidly evolving technology. A 3D phantom with complex 3D space curve designed in computer aided design (CAD) software can be easily and low-costly fabricated by 3D printing, so it is an ideal method for verifying 3D shape sensing.

In this paper, we demonstrate a large curvature radius 3D shape sensing using OFDR in multi-core fibers The strains on each core of the multi-core fiber measured by OFDR with three parallel channels are submitted to a Frenet-Serret frame to reconstruct a 3D shape of the fiber. We construct the theoretical model of strain measuring error and curvature radius reconstructing errors under different curvature radius. In the experiment, by this reconstructing errors model, we optimally select the measurable strain resolution and sensing spatial resolution to realize the shape reconstruction with a large curvature radius and reconstruct 2D circle shapes of curvature radius from 5 cm to 100 cm. The measured curvature radius reconstructing errors are agreed with the numerical stimulation results by the model. In addition, we present a 3D shape sensing validation method based on 3D printing technology. We design a 3D space curve with accurate space positions and fabricate it by 3D printing. By comparing between designed and reconstructed 3D space curves, we can evaluate the results of 3D shape sensing. In the experiment, we fabricate a 3D phantom contained a groove with a variable curvature radius of 5 cm to 100 cm. The presented distributed shape sensing system is used to reconstruct this complicated 3D shape. The root-mean-square error (RMSE) of curvature radius between the reconstructed and designed 3D space curves is 7.2 mm and the mean Euclidean distance is 3.4 mm.

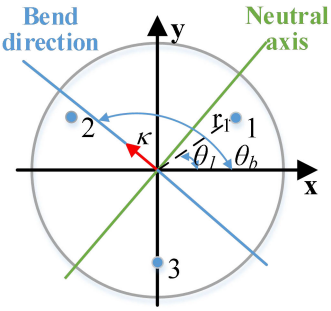

Fig. 1. Cross-sectional layout of a typical symmetric tri-core fiber.

II. Principle and Stimulation

A. Theoretical Model of Strain Measuring Errors and Curvature Radius Reconstructing Errors

A shape with different curvature radius causes different strain on fiber. A shape with a large curvature radius causes a very tiny strain on fiber. We need to choose an optimal strain measurement accuracy based on measurable curvature radius in the shape sensing. We firstly construct the theoretical model of strain measuring error and curvature radius reconstructing error. Here we use a Frenet-Serret frame method [19] to reconstruct 3D shape. If a multi-core fiber is bent in a given direction, different strain are generated on each core of the multi-core fiber. Fig. 1 describes a cross-sectional layout of a typical symmetric tri-core fiber. The bending-induced strain in each core of the multi-core fiber can be expressed as [19]:

$$\varepsilon_i = -\kappa r_i \cos(\theta_b - \theta_i), \tag{1}$$

where ε_i is the local induced strain on the i^{th} core. $r_i$is the distance between core i and the center of the multi-core fiber.κ is the curvature of a multi-core fiber. θ_b is the angular offset from the fiber bending direction to the local x-axis. θ_i is the angular offset from the core i to the local x axis.

For a symmetrically arranged tri-core fiber that are equally divided by a 120 degree offset at the same radial distance from the center of the multi-core fiber, namely, the curvature vector κ can be expressed as:

$$\kappa = \frac{2\sqrt{\left(\sum_{i=1}^{3} \varepsilon_i \cos\theta_i\right)^2 + \left(\sum_{i=1}^{3} \varepsilon_i sin\theta_i\right)^2}}{3r}. \tag{2}$$

Here $\kappa = 1/R$, where *R* is the bending curvature radius. Submit Eq. (1) to (2) and Eq. (2) can be expressed as:

$$R = \frac{3r}{2({\varepsilon_1}^2 + {\varepsilon_2}^2 + {\varepsilon_3}^2 - \varepsilon_1\varepsilon_2 - \varepsilon_2\varepsilon_3 - \varepsilon_1\varepsilon_3)^{1/2}}. \quad (3)$$

The reconstructing accuracy is related to the strain measurement accuracy. Based on Eq. (1)-(3), *R* is inversely proportional to ε_i. Reconstructing a shape with a large curvature radius requires for a high strain measurement accuracy. We apply the error transfer formula to obtain the relationship of the relative curvature radius reconstructing error and the strain measuring error as:

$$\frac{\Delta R}{R} = \frac{\partial \ln R}{\partial \varepsilon_1}\Delta\varepsilon_1 + \frac{\partial \ln R}{\partial \varepsilon_2}\Delta\varepsilon_2 + \frac{\partial \ln R}{\partial \varepsilon_3}\Delta\varepsilon_3, \quad (4)$$

where $\Delta\varepsilon_i$ is the strain measuring error on the i[th] core. ΔR is the reconstructing error of curvature radius. Submit Eq. (3) to (4) as:

$$\begin{aligned}\frac{\Delta R}{R} = {} & \frac{1}{2}\left|\frac{2\varepsilon_1-\varepsilon_2-\varepsilon_3}{{\varepsilon_1}^2 + {\varepsilon_2}^2 + {\varepsilon_3}^2 - \varepsilon_1\varepsilon_2 - \varepsilon_2\varepsilon_3 - \varepsilon_1\varepsilon_3}\right|\Delta\varepsilon_1 \\ & + \frac{1}{2}\left|\frac{2\varepsilon_2-\varepsilon_1-\varepsilon_3}{{\varepsilon_1}^2 + {\varepsilon_2}^2 + {\varepsilon_3}^2 - \varepsilon_1\varepsilon_2 - \varepsilon_2\varepsilon_3 - \varepsilon_1\varepsilon_3}\right|\Delta\varepsilon_2 \\ & + \frac{1}{2}\left|\frac{2\varepsilon_3-\varepsilon_1-\varepsilon_2}{{\varepsilon_1}^2 + {\varepsilon_2}^2 + {\varepsilon_3}^2 - \varepsilon_1\varepsilon_2 - \varepsilon_2\varepsilon_3 - \varepsilon_1\varepsilon_3}\right|\Delta\varepsilon_3. \end{aligned} \quad (5)$$

Submit Eq. (1) to (5) as:

$$\begin{aligned}\frac{\Delta R}{R} = {} & \left|\frac{2}{3\varepsilon_1}\sin^2(\theta_b - \theta_1)\right|\Delta\varepsilon_1 \\ & + \left|\frac{2}{3\varepsilon_1}\sin(\theta_b - \theta_1)\sin\left(\theta_b - \theta_1 - \frac{2\pi}{3}\right)\right|\Delta\varepsilon_2 \\ & + \left|\frac{2}{3\varepsilon_1}\sin(\theta_b - \theta_1)\sin\left(\theta_b - \theta_1 + \frac{2\pi}{3}\right)\right|\Delta\varepsilon_3, \end{aligned} \quad (6)$$

Assuming that$\Delta\varepsilon = \Delta\varepsilon_1 = \Delta\varepsilon_2 = \Delta\varepsilon_3$, Equation (6) can be expressed as:

$$\begin{aligned}\frac{\Delta R}{R} = {} & \left[\left|\sin^2(\theta_b - \theta_1)\right| + \left|\sin(\theta_b - \theta_1)\sin\left(\theta_b - \theta_1 - \frac{2\pi}{3}\right)\right| \right. \\ & \left. + \left|\sin(\theta_b - \theta_1)\sin\left(\theta_b - \theta_1 + \frac{2\pi}{3}\right)\right|\right]\frac{2\Delta\varepsilon}{3\left|\varepsilon_1\right|}, \end{aligned} \quad (7)$$

Submit Eq. (1) to (7) as:

$$\begin{aligned}\frac{\Delta R}{R} = {} & \left[\left|\sin\left(\theta_b - \theta_1 - \frac{2\pi}{3}\right)\right| + \left|\sin\left(\theta_b - \theta_1 - \frac{2\pi}{3}\right)\right| \right. \\ & \left. + \left|\sin\left(\theta_b - \theta_1 + \frac{2\pi}{3}\right)\right|\right]\frac{2R\Delta\varepsilon}{3r}. \end{aligned} \quad (8)$$

From Eq. (8), the relative curvature radius reconstructing error is in proportional to $\Delta\varepsilon$and *R*. Reconstructing a shape with a large curvature radius is required for a high strain measurement accuracy.

B. Measurable Strain Resolution, Strain Measuring Error and Sensing Spatial Resolution in OFDR

From analysis in Section IIA, we find that reconstructing a shape with a lower $\Delta R/R$ requires decreasing strain measuring error $\Delta\varepsilon$. $\Delta\varepsilon$ is difficult to acquire directly which is related to noise of the OFDR system. We firstly analyze the measurable strain variation resolution ε_{min}, which is related to the optical frequency resolution $\delta f_{\min}$. ε_{min} can be expressed as [25]:

$$\varepsilon_{\min} = \delta f_{\min}/K = \Delta F/K(M+N), \quad (9)$$

where *N* is data points of the sliding widow for dividing local segment in the spatial domain, which is related to the sensing spatial resolution ΔX based on the relation of $\Delta X = N\Delta Z$ and ΔZ is the spatial resolution of one data point. *M* is the spectrum interpolation factor for each local segment. *K* is the coefficient of the shift of RBS v. s. strain. ΔF is the optical frequency tuning range of the tunable laser source (TLS).

In the DSS, ΔX is need to be minimized for high accuracy shape reconstruction [13]. From Eq. (9), ε_{min} can be improved without sacrificing ΔX by increasing *M*, which is benefit to shape reconstruction with a large curvature radius. The strain measuring error $\Delta\varepsilon$ is correlated to ε_{min}. However, $\Delta\varepsilon$ cannot be improved infinitely by increasing *M*, which is finally limited to the noise margin contributed by TLS's wavelength stability, signal to noise ratio (SNR) of RBS and environment noise. In addition, over size *M* can increase computational burden and decrease the stability of strain measurement [26], [27]. When increasing *M* cannot decrease $\Delta\varepsilon$, we can increase *N* to decrease $\Delta\varepsilon$further. More effective data in the spatial domain can realize a higher SNR of local RBS, but it will deteriorate ΔX based on the relation of $\Delta X = N\Delta Z$. For above, when the OFDR system and multi-core fiber are determined, we only optimally choose these two parameters of ΔX and $\varepsilon_{\min}$ based on the requirement of DSS.

C. Numerical Stimulation of Relationship of the Strain Measuring Error and the Curvature Radius Reconstructing Error

To acquire the numerical relationship between the strain measuring error $\Delta\varepsilon$ versus the relative curvature radius reconstructing error $\Delta R/R$, we perform a numerical simulation to analyze the reconstructing error model of Eq. (8) in different curvature radii. From Eq. (8), $\theta_b - \theta_1$ will lead to different strain distribution of the three cores in multi-core fiber. When $\theta_b - \theta_1 = \pi/2$, $\Delta R/R$ is the maximum. Here we set $\theta_b - \theta_1 = \pi/2$, $\Delta\varepsilon$= 0$\sim$30 $\mu\varepsilon$ and $R = 0.14$ m to 1 m. The numerical stimulation results are shown in Fig. 2. The slopes of curves are in proportional to curvature radii, which reflects that reconstructing a shape with a larger curvature radius requires a lower strain error. When $R = 0.14$ m, the $\Delta R/R$can be under 5% at the condition of $\Delta\varepsilon$<11 $\mu\varepsilon$. When $R = 1$ m, the $\Delta R/R$ can be under 5% at the condition of $\Delta\varepsilon$<1.58 $\mu\varepsilon$. Based on the numerical stimulation results shown in Fig. 2 and the model of Eq. (8), we can acquire $\Delta\varepsilon$ based on the requirement of $\Delta R/R$ and *R*. In the optimizing strategy of the DSS, ΔX is firstly set to a minimized value based on the requirement of strain measurement. We need to know the

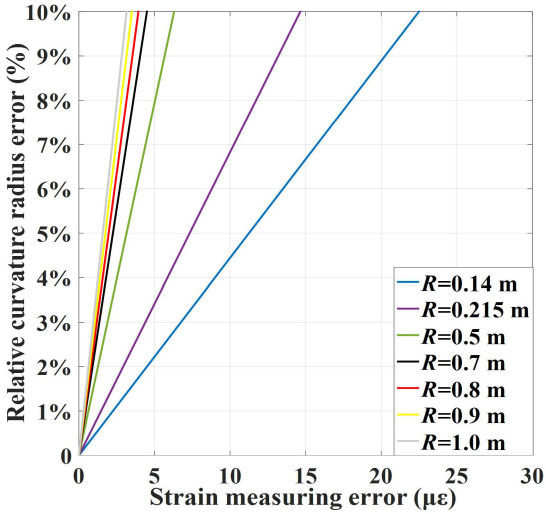

Fig. 2. Numerical simulation results of strain measuring error versus relative curvature radius reconstructing error in different curvature radii.

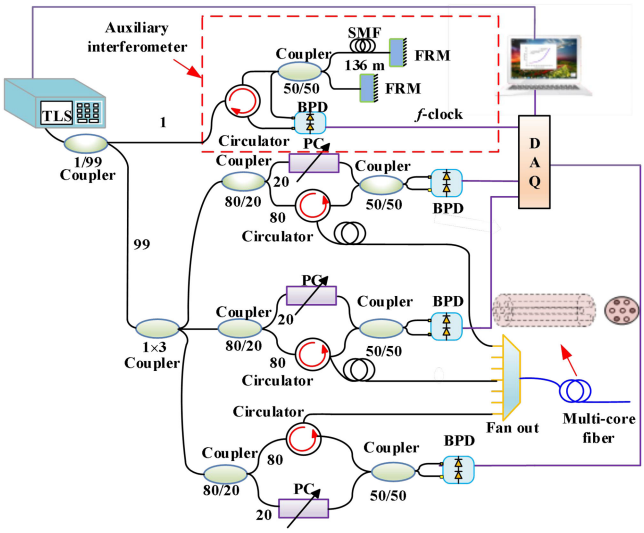

Fig. 3. Configuration of distributed shape sensing based on three parallel channels OFDR. TLS is tunable laser source. PC is Polarization controller. FRM is faraday rotating mirror. BPD is balanced photo-detector. DAQ is data acquisition card. The device of fan out is used to break out each core of a multi-core fiber to enable each core to be addressed independently through single-mode fiber pigtails. The three parallel channels consists of three Mach-Zehnder interferometer, which sample arm is connected to the three core of the multi-core fiber.

requirement of $\Delta R/R$and R to acquire the requirement of $\Delta\varepsilon$ based on Eq. (8) shown in Fig. 2 and then setting a similar ε_{min} by choosing a corresponding M. If simply increasing M cannot acquire the requirement of $\Delta\varepsilon$, we will increase N namely increase the value of ΔX.

III. Experiments and Discussion

A. OFDR System Configuration

The DSS system based on three parallel channels OFDR are shown in Fig. 3. The tuning speed, tuning range and starting wavelength of the tunable laser source (TLS, Keysight 81607A) are 1×10^4 GHz/s (80 nm/s), 5.5×10^3 GHz (44 nm) and 1550 nm, respectively. A 1: 99 coupler is used to split the light from the TLS into the main and auxiliary interferometers. The 1% light is sent to an auxiliary interferometer that provides an external clock (f-clock) to trigger data acquisition card (DAQ) to realize even optical frequency sampling sample for main interference signals enabling to eliminate the nonlinear tuning effect of TLS. This auxiliary interferometer is polarization-insensitive owing to a Michelson interferometer structure with two faraday rotating mirrors (FRMs) and its delay fiber's length is 136 m. The 99% light is sent to the main interferometer part, which consists of three Mach-Zehnder interferometer as three parallel channels by a 13 coupler. In each Mach-Zehnder interferometer, the input light is separated by a 20:80 coupler, in which 20% of the light is send to the reference arm, and 80% of the light is sent to the test arm. The light of the test arm is sent to the pigtail of the device of fan out through a circulator. The fan out (Yangtze Inc. FAN-7-42) is used to break out each core of a multi-core fiber to enable each core to be addressed independently through single-mode fiber pigtails. The multi-core fiber under test is 7 core multi-core fiber with a cladding diameter of 150 μm and the core spacing of 41.5 μm, designed for 1550 nm. (Yangtze Inc. MCF 7-42/250SM). Three cores symmetrically arranged at a 120 degree offset in the multi-core fiber are used. The Rayleigh backscattering from different positions of multi-core fiber is sent to interfere with the reference light directly from TLS in a coupler detected by balanced photo-detectors (BPD) and then the electrical signals are sent to DAQ. In this OFDR, the spatial resolution of one data point $\Delta Z$is 18 μm based on $\Delta F = 5.5\times10^3$ GHz [25].

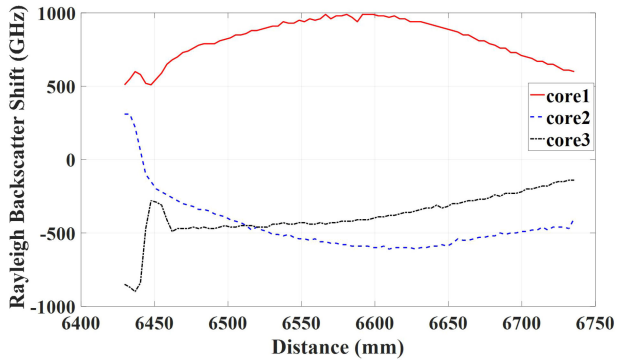

Fig. 4. Distributed optical frequency shifts of Rayleigh backscattering spectra along the multi-core fiber when the multi-core fiber is placed as a circle with a radius of 5 cm. These three curves represent optical frequency shifts of the three cores in the multi-core fiber, respectively.

B. Reconstruction Results About 2D Shape With a Small Curvature Radius

We firstly show the optical frequency shifts of RBS along the multi-core fiber when the multi-core fiber is placed as a circle with a radius of 5 cm in Fig. 4. Here the segment length N is chosen to be 200, which is corresponding to the effective sensing spatial resolution $\Delta X = 3.6$ mm. Here $\Delta X = 3.6$ mm is

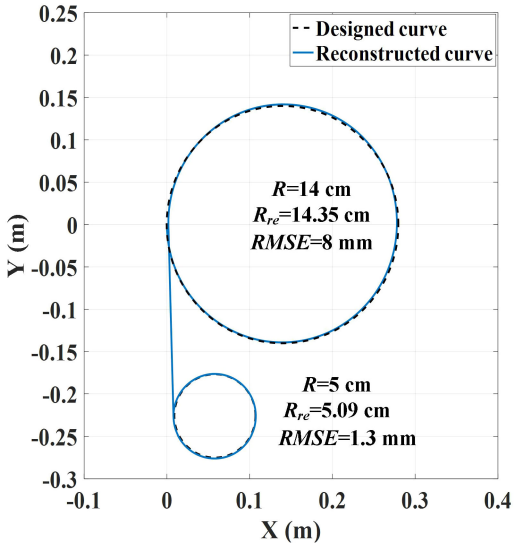

Fig. 5. Reconstruction result of two 2D circle shapes with radii of 5 cm and 14 cm.

minimized based on this SNR of this system. From Fig. 4, we find that optical frequency shifts of the three cores in the multi-core fiber are different. The shifts of core 1 are positive values and the shifts of core 2 and core 3 are negative values. Optical frequency shifts distribution can be converted to strains distribution by the coefficient of RBS v. s. strain *K*. The positive and negative values of optical frequency shifts represents stretching strain and compression strain, respectively. The strain distribution of these three cores are submitted to Frenet-Serret frame and then the shape can be reconstructed. The reconstruction result of a circle with a radius of 5 cm shown in Fig. 5. The coefficient of RBS v. s. strain *K* is a significant parameter. We acquire *K* by reconstructing a circular shape with a known curvature radius. Here the known shape is a 2D circle with a radius of 5 cm. *K* is calculated to be 8.0 $\mu\varepsilon$/GHz that is agreed with the calibration coefficient in [11].

We firstly reconstruct a 2D circle with a relatively small curvature radius of 14 cm, 21.5 cm and 50 cm. Here $\Delta X=$ 3.6 mm is minimized based on this SNR of this system by setting $N = 200$. If $\Delta R/R$ is needed to be less than a certain value, we need to set a reasonable ε_{min} namely *M* based on the reconstructing error model of Eq. (8). For example, for a circle with a curvature radius of 14 cm, if $\Delta R/R$ is needed to be ensured to under 5%, $\Delta\varepsilon$ is needed to be ensured to under 11 $\mu\varepsilon$ based on the numerical stimulation results shown in Fig. 2. When *M* is set to 3800, ε_{min} is 11 $\mu\varepsilon$. The reconstructed two 2D circle shape curves with radii of 5 cm and 14 cm are shown in Fig. 5. The mean reconstructed curvature radius of this circle is 14.35 cm. We calculate the relative error of reconstructing curvature radius $\Delta R/R$ based on this relation as:

$$\Delta R/R = \frac{|R_{re} - R|}{R} \times 100\%, \tag{10}$$

where R_{re} and *R* are the reconstructed and designed value of curvature radius of reconstructed shape, respectively. Based on Eq. (10), the relative error of a reconstructed 2D circle with a radius of 14 cm is about 2.5%, which is under 5%. We also calculate the root-mean-square error (RMSE) of curvature radius based on the formula as:

$$RMSE = \sqrt{\frac{\sum_{i=1}^{n} \left(R_{re,i} - R_{de,i}\right)^2}{n}}, \tag{11}$$

where $R_{re,i}$ and $R_{de,i}$ are reconstructed and designed curvature radius at the position *i* along the multi-core fiber, respectively. The *RMSE* of the reconstructed 2D circle shapes with radii of 5 cm and 14 cm are 1.3 mm and 8 mm, respectively. We also reconstruct 2D circle with curvature radii of and the results shown in Table I. The choices of *M* are also based on the numerical stimulation results shown in Fig. 2. $\Delta R/R$ about 2D circle shapes of 21.5 cm and 50 cm are 2.7% and 4.0%, respectively, which are under 5%. The relationship between $\Delta R/R$ and ε_{min} shown in Table I is closed to the relation of $\Delta R/R$ and $\Delta\varepsilon$ shown in Fig. 2, which verifies the model of Eq. (8) is feasible. We can acquire the requirement of based on the requirement of $\Delta R/R$and *R* and then set a similar ε_{min} by choosing a corresponding *M*.

TABLE I
RECONSTRUCTION RESULTS ABOUT 2D CIRCLE SHAPE WITH A SMALL CURVATURE RADIUS

R (cm)	*N*	ΔX (mm)	*M*	δf_{min} (GHz)	ε_{min} (με)	R_{re} (cm)	ΔR / *R*
14	200	3.6	3800	1.375	1.1	14.35	2.5 %
21.5	200	3.6	5800	0.916	7.328	22.7	2.7 %
50	200	3.6	10000	0.539	4.312	52.0	4.0 %

TABLE II
RECONSTRUCTION RESULTS ABOUT 2D CIRCLE SHAPE WITH A CURVATURE RADIUS OF 70 cm

N	ΔX (mm)	*M*	δf_{min} (GHz)	ε_{min} (με)	R_{re} (cm)	ΔR / *R*
200	3.6	20000	0.272	2.176	72.9	4.1 %
200	3.6	40000	0.137	1.096	72.0	2.9 %
200	3.6	80000	0.0686	0.549	73.1	4.4 %

C. Reconstruction Results About 2D Shape With a Large Curvature Radius

We also reconstruct 2D circle shapes with a large curvature radius. Here $\Delta X=$ 3.6 mm is minimized based on this SNR of this system by setting $N = 200$. For reconstructing 2D shape with a large curvature radius, *M* should be increased greatly to ensure $\Delta R/R$ satisfying the requirements. The total results of 2D circle shape with a curvature radius of 70 cm are shown in Table II. Based on the numerical stimulation results shown in Fig. 2, $\Delta\varepsilon$should be under 2.2 $\mu\varepsilon$ if $\Delta R/R$ is under 5%. Therefore, *M* is firstly set to 20000 and $\varepsilon_{min} = 2.18$ $\mu\varepsilon$. The reconstruction results show that $R_{re}=$ 72.9 cm and $\Delta R/R$ is 4.1%. When ε_{min} is improved to 1.1 $\mu\varepsilon$ by setting $M = 40000$, $\Delta R/R$ is 2.9%. When ε_{min} is improved to 0.549 $\mu\varepsilon$ by setting $M = 80000$, $\Delta R/R$ is rebound to 4.4%, which is not decreased

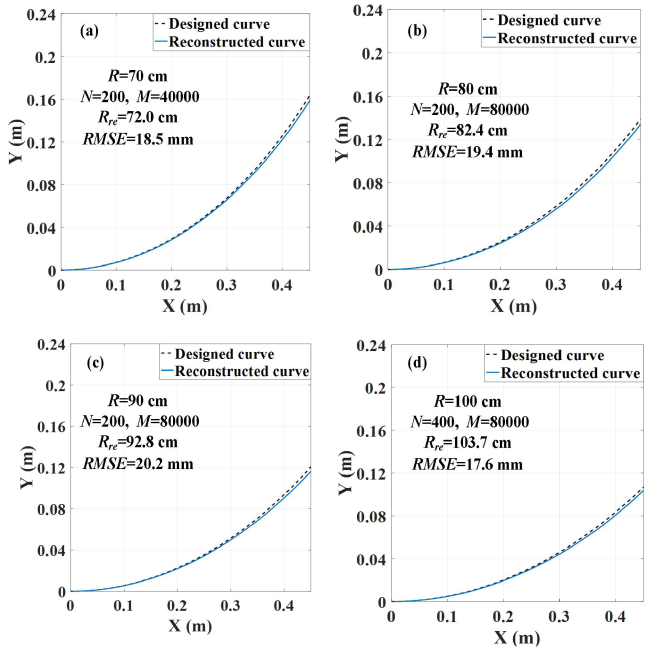

Fig. 6. Reconstruction results of a 2D circle shape with a radius of (a) 70 cm, (b) 80 cm, (c) 90 cm and (d) 100 cm.

TABLE III
RECONSTRUCTION RESULTS ABOUT 2D CIRCLE SHAPE WITH A CURVATURE RADIUS OF 80 cm

N	ΔX (mm)	M	δf_{min} (GHz)	ε_{min} (με)	R_{re} (cm)	ΔR / R
200	3.6	2000	0.272	2.176	84.3	5.4 %
200	3.6	40000	0.137	1.096	82.6	3.3 %
200	3.6	80000	0.0686	0.549	82.4	3.0 %
200	3.6	100000	0.0549	0.439	84.7	5.9 %

along with ε_{min} decreasing. The reason is that $\Delta\varepsilon$ is closed to the noise margin of this OFDR system and cannot be decreased further by increasing *M*. The optimal reconstructed circle shape curve with a ΔX= 3.6 mm (N = 200) and ε_{min} = 1.096 $\mu\varepsilon$ (M = 40000) shown in Fig. 6(a) and the *RMSE* is 18.5 mm.

The total results of 2D circle shape with a curvature radius of 80 cm are shown in Table III. Based on the stimulation results shown in Fig. 2, when R = 80 cm and $\Delta R/R$ <5%, $\Delta\varepsilon$ is under 2 $\mu\varepsilon$. Therefore, M is firstly set to 20000 and ε_{min} = 2.18 $\mu\varepsilon$. The reconstruction results show that R_{re}= 84.3 cm and the $\Delta R/R$ is 5.4%, which is a little higher than the requirement of $\Delta R/R$<5%. When ε_{min} is improved to 1.096 $\mu\varepsilon$ by setting M = 40000, $\Delta R/R$ is 3.3%, which is under 5%. When ε_{min} is improved to 0.549 $\mu\varepsilon$ by setting M = 80000, $\Delta R/R$ is 3.0%, which is not improved greatly due to the noise margin of this OFDR system. When ε_{min} is improved to 0.439 $\mu\varepsilon$ by setting M = 100000, $\Delta R/R$ is rebound to 5.9% due to over size M decreasing the stability of strain measurement. The optimal reconstructed circle shape curve with a ΔX= 3.6 mm (N = 200) and ε_{min} = 0.549 $\mu\varepsilon$ (M = 80000) shown in Fig. 6(b) and the *RMSE* is 19.4 mm.

TABLE IV
RECONSTRUCTION RESULTS ABOUT 2D CIRCLE SHAPE WITH A CURVATURE RADIUS OF 90 cm

N	ΔX (mm)	M	δf_{min} (GHz)	ε_{min} (με)	R_{re} (cm)	ΔR / R
200	3.6	20000	0.272	2.176	100.2	11.3 %
200	3.6	40000	0.137	1.096	94.5	5.0 %
200	3.6	80000	0.0686	0.549	92.8	3.1 %
200	3.6	100000	0.0549	0.439	93.4	3.8 %

TABLE V
RECONSTRUCTION RESULTS ABOUT 2D CIRCLE SHAPE WITH A CURVATURE RADIUS OF 100 cm

N	ΔX (mm)	M	δf_{min} (GHz)	ε_{min} (με)	R_{re} (cm)	ΔR / R
200	3.6	40000	0.137	1.096	114.5	14.5 %
200	3.6	80000	0.0686	0.549	105.2	5.2 %
200	3.6	100000	0.0549	0.439	106.9	6.9 %
400	7.2	40000	0.136	1.088	105.4	5.4 %
400	7.2	80000	0.0684	0.547	103.7	3.7 %
400	7.2	120000	0.0457	0.366	105.6	5.6 %

The results of 2D circle shape reconstruction with a curvature radius of 90 cm are shown in Table IV. Based on the numerical stimulation results shown in Fig. 2, when R = 80 cm and $\Delta R/R$<5%, $\Delta\varepsilon$should be under 1.75 $\mu\varepsilon$. Therefore, M is firstly set to 40000 and ε_{min} = 1.096 $\mu\varepsilon$. The reconstruction results show that $\Delta R/R$ is 5%. We also show the results of M = 20000 and $\Delta R/R$, which are deteriorated greatly to 5.2%. This phenomena reflects the $\Delta R/R$is more sensitive when R is relatively larger. When ε_{min} is improved to 0.549 $\mu\varepsilon$ by setting M = 80000, $\Delta R/R$ is 3.0%. When ε_{min} is improved to 0.439 $\mu\varepsilon$ by setting M = 100000, $\Delta R/R$ is rebound to 3.8%. When M = 80000, ε_{min} = 0.549 $\mu\varepsilon$ that is closed to the minimal measurable strain variation of this OFDR system under the condition of ΔX= 3.6 mm (N = 200) and this value is similar to the results of 2D circle shape reconstruction with a curvature radius of 80 cm. The optimal reconstructed circle shape curve with a ΔX= 3.6 mm (N = 200) and ε_{min} = 0.549 $\mu\varepsilon$ (M = 80000) shown in Fig. 6(c) and the *RMSE* is 20.2 mm.

The results of 2D circle shape reconstruction with a curvature radius of 100 cm are shown in Table V. Here ΔX is also firstly minimized to 3.6 mm based on this SNR of this system by setting N = 200. Based on the numerical stimulation results shown in Fig. 2, when R = 100 cm and $\Delta R/R$<5%, $\Delta\varepsilon$should be under 1.58 $\mu\varepsilon$. Therefore, M is firstly set to 40000 and ε_{min} = 1.096 $\mu\varepsilon$. The reconstruction result show that $\Delta R/R$ is 14.5%, which reflects that serious reconstructing error can be generated even at a small strain measuring error when R = 100 cm. When $\varepsilon_{\min}$ is improved to 0.549 $\mu\varepsilon$ by setting M = 80000, $\Delta R/R$is 5.2%, which is a little big. When ε_{min} is improved to 0.439 $\mu\varepsilon$ by setting M = 100000, $\Delta R/R$ is rebound to 5.9%. The strain measuring error $\Delta\varepsilon$ cannot be improved infinitely by increasing M, which is finally limited to the noise margin of the system. To decrease $\Delta\varepsilon$ further, we need to sacrifice ΔX and we secondly set to be 7.2 mm by setting N = 400. M is firstly set

to 40000 and $\varepsilon_{min} = 1.088\ \mu\varepsilon$. The reconstruction result show that $\Delta R/R$is 5.4%. We continually increase *M* to be 80000 and $\varepsilon_{min} = 0.547\ \mu\varepsilon$. The reconstruction result show that $\Delta R/R$ is 3.7%. We continually increase *M* to be 100000 and $\varepsilon_{min} = 0.439\ \mu\varepsilon$. The reconstruction result show that $\Delta R/R$ is rebound to 5.6%. When $M = 80000$, $\varepsilon_{min} = 0.547\ \mu\varepsilon$ that is closed to the minimal measurable strain variation of this OFDR system under the condition of $\Delta X = 7.2$ mm ($N = 400$). Compared with the reconstruction results of $\Delta X = 3.6$ mm and $\Delta X = 7.2$ mm, sacrificing ΔXcan improve the reconstruction accuracy, but it also can influence the complex shape reconstruction when the is required to be very tiny value. The optimal reconstructed circle shape curve with a $\Delta X = 7.2$ mm ($N = 400$) and $\varepsilon_{min} = 0.547\ \mu\varepsilon$ ($M = 80000$) shown in Fig. 6(d) and the *RMSE* is 17.6 mm.

For above, the experimental results of Table I to IV verify that the effectiveness of the reconstructing error model of Eq. (8) and the optimizing strategy for choosing *M* and *N*. We can choose a reasonable *M* based on a similar ε_{min} corresponding to $\Delta\varepsilon$the requirement of $\Delta R/R$and *R* in Fig. 2. We can continually decrease ε_{min} to decrease $\Delta R/R$ further, but the minimal $\Delta R/R$ is finally limited by the noise margin of this OFDR system. Based on the reconstruction results in Table I to III, when $\varepsilon_{min} = 0.549\ \mu\varepsilon$ by setting $M = 80000$, $\Delta\varepsilon$ is limited by the noise margin of this OFDR system under the condition of $\Delta X = 3.6$ mm ($N = 200$). Sacrificing can decrease the noise margin of this OFDR system. Based on the reconstruction results in Table IV, when $\varepsilon_{min} = 0.547\ \mu\varepsilon$ by setting $M = 80000$, $\Delta\varepsilon$is limited by noise margin of this OFDR system under the condition of $\Delta X = 7.2$ mm ($N = 400$). Based on the noise margin of this OFDR, we can acquire the maximal reconstructed curvature radius in this OFDR, which is very important information for 3D shape sensing with a high accuracy.

D. Complicated 3D Shape With Large Curvature Radius Reconstruction

3D shape reconstruction is the core point for shape sensing. We will use the theatrical model, the numerical stimulation results and the optimal sensing parameters from experimental results of 2D shape circles resolution in Section II, III-B and III-C to guide 3D shape with large curvature radius reconstruction. To verify the reconstruction ability for 3D shape using the presented method, we present a 3D shape sensing validation method based on 3D printing technology. We can design a 3D space curve with accurate space positions and fabricate it by 3D printing. By comparing between designed and reconstructed 3D space curves, we can evaluate the results of 3D shape sensing. In the experiment, we design a 3D phantom contained a groove with variable curvature radii of 5 cm to 100 cm by 3D CAD software (Solidworks, Dassault Systèmes SOLIDWORKS Corp.) shown in Fig. 7(a). The phantom has two parts. One part is a part of cone with variable curvature radii from 70 cm to 100 cm. Other part is a cylinder with a radius of 5 cm. We design a 0.5 mm × 0.5 mm groove on the phantom. The groove on the cone part can generate a space curve with variable curvature radii from 70 cm to 100 cm. The groove on the cylinder part is

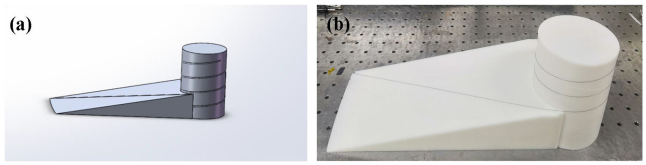

Fig. 7. 3D phantom contained a groove with a variable curvature radius of 5 cm to 100 cm. (a) Solidworks' 3D drawing. (b) Phantom by 3D printing. The phantom has two parts. One part is a part of cone with variable radii from 70 cm to 100 cm. Other part is a cylinder with a radius of 5 cm. A 0.5 mm 0.5 mm groove is contained on the phantom. The groove on the cone part can generate a space curve with variable curvature radii from 70 cm to 100 cm.

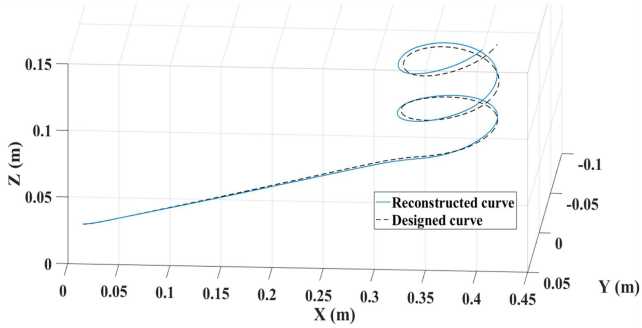

Fig. 8. Reconstructing results of the 3D phantom contained a groove with variable curvature radii of 5 cm to 100 cm by 3D printing. The solid line is the reconstructed 3D curve. The dash line is designed 3D curve.

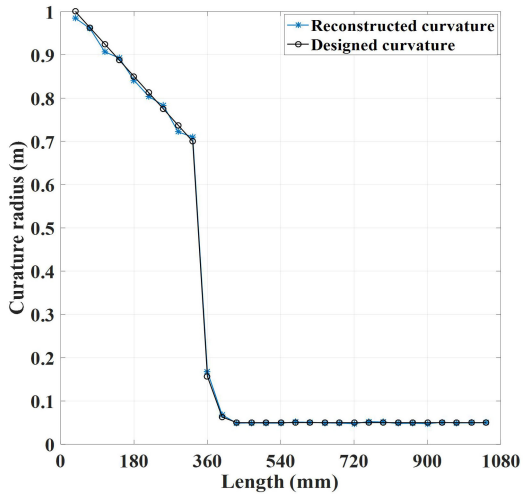

Fig. 9. Curvature radii of the designed and reconstructed 3D space curves along the multi-core fiber length.

a space spiral with a curvature radius of 5 cm. We can acquire the space curve with accurate space position coordinates from Solidworks. We fabricate this 3D phantom by 3D printing based on Solidworks drawing and the photograph is shown in Fig. 7(b). Here the working accuracy of this 3D printing is ±0.15 mm.

We use the presented distributed shape sensing system to reconstruct this 3D phantom by 3D printing. Since the maximal curvature radius of this phantom is 100 cm, we choose $\Delta X = 7.2$ mm and $\varepsilon_{min} = 0.547\ \mu\varepsilon$ ($N = 400$, $M = 80000$)

TABLE VI
RMSE OF CURVATURE RADIUS AND EUCLIDEAN DISTANCE OF THE 3D SHAPE RECONSTRUCTION RESULTS

	ΔX =3.6 mm ε_{min}=2.176 με N=200, M=20000	ΔX =3.6 mm ε_{min}=2.176 με N=200,M=40000	ΔX =3.6 mm ε_{min}=0.549 με N=200, M=80000	ΔX =7.2 mm ε_{min}=0.547 με N=400, M=80000
RMSE of curvature radius	23.6 mm	13.8 mm	8.4 mm	7.2 mm
Mean Euclidean distance	7.8 mm	6.4 mm	5.7 mm	3.4 mm
Maximal Euclidean distance	15.8 mm	12.5 mm	10.4 mm	6.3 mm

as the demodulation parameters in OFDR based on numerical stimulation and experimental results of Section II-C and III-B. The reconstructed 3D shape is shown in Fig. 8. We also show curvature radii of the designed and reconstructed 3D space curves along the multi-core fiber length in Fig. 9. The designed and reconstructed 3D space curves are agreed well. *RMSE* of curvature radius is 7.2 mm. We also calculate Euclidean distance between designed and reconstructed 3D space curves along the multi-core fiber. The mean Euclidean distance is 3.4 mm and the maximal Euclidean distance is 6.3 mm. We also apply different ΔX and ε_{min} to reconstruct this 3D phantom. The *RMSE* of curvature radius and Euclidean distance of the reconstructed results shown in Table VI. From Table VI, the reconstructed results with $\Delta X =$ 7.2 mm and $\varepsilon_{min} = 0.547\ \mu\varepsilon$ has the best results, which are agreed with the experiment and numerical stimulation results of Section II-C and III-B.

Since we only use the common multi-core fiber for 3D shape sensing, the twist along the multi-core fiber is a significant error source for 3D shape reconstruction. The twist can induce strain and torsion error [28], [29]. We use the groove on 3D phantom to fix optical fiber with the model but don't use tape or other fixing tools, which can avoid external force and keep the fiber at its natural shape. This method can mitigate the impact of torsion on shape reconstruction. In the future, we will consider to apply helical multi-core fiber to reduce the twist effect [17], [30]. In addition, bending and twisting of the multi-core fiber can be measured by the local variations of the group and phase propagation [31], which is a possible method to compensate the twist effect on multi-core fiber.

IV. CONCLUSION

We demonstrate a large curvature radius shape sensing based on OFDR. We construct a theoretical model of strain measuring error and curvature radius reconstructing errors under different curvature radius. We perform a numerical stimulation to this model. In experiments, by this reconstructing errors model, we optimally select the measurable strain resolution and sensing spatial resolution to realize the shape reconstruction with a large curvature radius and reconstruct 2D circle shapes of curvature radius from 5 cm to 100 cm. The measured curvature radius reconstructing errors are agreed with the numerical stimulation results by the model. The noise margin of this OFDR can be measured by 2D circle shapes reconstruction with large curvature radius. Based on this noise margin of this OFDR, we can acquire the maximal reconstructed curvature radius in this OFDR, which is very important information for high accuracy 3D shape sensing. In 3D shape reconstruction with a large curvature radius, we firstly present a 3D shape sensing validation method based on 3D printing technology. We can design a 3D space curve with accurate space positions and fabricate it by 3D printing. By comparing between designed and reconstructed 3D space curves, we can evaluate the results of 3D shape sensing. We fabricate a 3D phantom contained a groove with a variable curvature radius of 5 cm to 100 cm. The presented distributed shape sensing system is used to reconstruct this complicated 3D shape. The *RMSE* of curvature radius between the reconstructed and designed 3D space curves is 7.2 mm and mean Euclidean distance is 3.4 mm. In future, the multi-core fiber is used to telecommunication, so Rayleigh backscattering of each core is very low. We will consider to use Rayleigh scattering enhanced multi-core fiber or continuous grating multi-core for DSS, which will be benefit to increase SNR of OFDR and enhance the sensitivity of DSS. In addition, the torsion is also a significant parameter for 3D space curve reconstruction besides the curvature. We will focus on the torsion measurement in the following studies. We also will consider to apply helical multi-core fiber to reduce the twist effect.

REFERENCES

[1] M. Amanzadeh, S. M. Aminossadati, M. S. Kizil, and A. D. Rakić, "Recent developments in fibre optic shape sensing," *Measurement*, vol. 128, pp. 119–137, 2018.
[2] F. Parent *et al.*, "Enhancement of accuracy in shape sensing of surgical needles using optical frequency domain reflectometry in optical fibers," *Biomed. Opt. Exp.*, vol. 8, no. 4, pp. 2210–2221, 2017.
[3] H. Wang, R. Zhang, W. Chen, X. Liang, and R. Pfeifer, "Shape detection algorithm for soft manipulator based on fiber Bragg gratings," *IEEE/ASME Trans. Mechatron.*, vol. 21, no. 6, pp. 2977–2982, Dec. 2016.
[4] A. Cusano *et al.*, "Experimental modal analysis of an aircraft model wing by embedded fiber Bragg grating sensors," *IEEE Sens. J.*, vol. 6, no. 1, pp. 67–77, Feb. 2006.
[5] B. Joseph, K. Justin, F. Mark, S. Eric, and G. Dawn, "Fiber optic strain, temperature and shape sensing via OFDR for ground, air and space applications," *Proc. SPIE*, vol. 8876, 2013, Art. no. 887614.
[6] K. Hoehn, A. Olsson, and J. W. Arkwright, "High capacity torque and compression measurements using fibre optic sensors," in *Proc. 2nd Int. Conf. Fibre-Optic Photon. Sens. Ind. Saf. Appl.*, 2017, pp. 39–44.
[7] S. M. Aminossadati, M. Amanzadeh, E. Prochon, J. Kok, and S. Adam, "Step change approaches in coal technology and fugitive emissions research," *Int. J. Mining Sci. Technol.*, vol. 24, no. 3, pp. 363–367, 2014.
[8] H. Moon, J. Jeong, S. Kang, K. Kim, Y.-W. Song, and J. Kim, "Fiber-Bragg-grating-based ultrathin shape sensors displaying single-channel sweeping for minimally invasive surgery," *Opt. Laser Eng.*, vol. 59, pp. 50–55, 2014.
[9] Z. Zhao, M. A. Soto, M. Tang, and L. Thévenaz, "Distributed shape sensing using brillouin scattering in multi-core fibers," *Opt. Exp.*, vol. 24, no. 22, pp. 25211–25223, 2016.
[10] Ł. Szostkiewicz *et al.*, "High-resolution distributed shape sensing using phase-sensitive optical time-domain reflectometry and multicore fibers," *Opt. Exp.*, vol. 27, no. 15, pp. 20763–20773, 2019.
[11] S. T. Kreger, D. K. Gifford, M. E. Froggatt, B. J. Soller, and M. S. Wolfe, "High resolution distributed strain or temperature measurements in single-

and multi-mode fiber using swept-wavelength interferometry," in *Proc. Opt. Fiber Sensors*, 2006, Art. no. ThE42.

[12] M. Froggatt and J. Moore, "High-spatial-resolution distributed strain measurement in optical fiber with Rayleigh scatter," *Appl. Opt.*, vol. 37, no.no. 10, pp. 1735–1740, 1998.

[13] R. G. Duncan *et al.*, "High-accuracy fiber-optic shape sensing," in *Proc. Sens. Syst. Netw.: Phenomena Technol. Appl. NDE Health Monit.*, 2007, Art. no. 65301S.

[14] F. Parent *et al.*, "Intra-arterial image guidance with optical frequency domain reflectometry shape sensing," *IEEE Trans. Med. Imag.,* vol. 38, no. 2, pp. 482–492, Feb. 2019.

[15] C. Shao *et al.*, "OFDR with local spectrum matching method for optical fiber shape sensing," *Appl. Phys. Exp.*, vol. 12, no.no. 8, 2019, Art. no. 082010.

[16] S. Zhao, J. Cui, C. Yang, Z. Ding, and J. Tan, "Simultaneous measurement of shape and temperature in the substrate-attaching-fibers sensing system," *IEEE Photon. J.*, vol. 9, no. 6, Dec. 2017, Art. no. 6805008.

[17] G. Yin *et al.*, "Distributed directional torsion sensing based on an optical frequency domain reflectometer and a helical multicore fiber," *Opt. Exp.*, vol. 28, no. 11, pp. 16140–16150, 2020.

[18] Z. Guo, C. Xing, C. Ke, K. Yang, and D. Liu, "3D shape sensing utilizing SBS in multi-core fiber," in *Proc. Opt. Fiber Commun. Conf.*, 2019, Art. no. W1C.7.

[19] J. P. Moore and M. D. Rogge, "Shape sensing using multi-core fiber optic cable and parametric curve solutions," *Opt. Exp.*, vol. 20, no. 3, pp. 2967–2973, 2012.

[20] A. Zafeiropoulou, A. Masoudi, A. Zdagkas, L. Cooper, and G. Brambilla, "Curvature sensing with a D-shaped multicore fibre and brillouin optical time-domain reflectometry," *Opt. Exp.*, vol. 28, no.no. 2, pp. 1291–1299, 2020.

[21] X. Chen, X. Yi, J. Qian, Y. Zhang, L. Shen, and Y. Wei, "Updated shape sensing algorithm for space curves with FBG sensors," *Opt. Laser. Eng*, vol. 129, 2020, Art. no. 106057.

[22] J. P. Moore, M. D. Rogge, and T. W. Jones, "Photogrammetric verification of fiber optic shape sensors on flexible aerospace structures," in *Proc. IEEE Avion. Fiber-Opt. Photon. Dig. CD*, 2012, pp. 9–10.

[23] Y. L. Park *et al.*, "Real-time estimation of 3-D needle shape and deflection for MRI-guided interventions," *IEEE/ASME Trans. Mechatron.*, vol. 15, no. 6, pp. 906–915, Dec. 2010.

[24] S. Jäckle, T. Eixmann, H. Schulz-Hildebrandt, G. Hüttmann, and T. Pätz, "Fiber optical shape sensing of flexible instruments for endovascular navigation," *Int. J. Comput. Ass. Rad.*, vol. 14, pp. 2137–2137, 2019.

[25] Z. Ding *et al.*, "Distributed optical fiber sensors based on optical frequency domain reflectometry: A review," *Sensors*, vol. 18, no. 4, 2018, Art. no. 1072.

[26] J. Cui, S. Zhao, D. Yang, and Z. Ding, "Investigation of the interpolation method to improve the distributed strain measurement accuracy in optical frequency domain reflectometry systems," *Appl. Opt.*, vol. 57, no. 6, pp. 1424–1431, 2018.

[27] Y. Du, S. Jothibasu, Y. Zhuang, C. Zhu, and J. Huang, "Rayleigh backscattering based macrobending single mode fiber for distributed refractive index sensing," *Sens. Actuat. B Chem.*, vol. 248, pp. 346–350, 2017.

[28] R. Xu, A. Yurkewich, and R. V. Patel, "Curvature, torsion, and force sensing in continuum robots using helically wrapped FBG sensors," *IEEE Robot. Autom. Lett.*, vol. 1, no. 2, pp. 1052–1059, Jul. 2016.

[29] J. P. Moore, "Shape sensing using multi-core fiber," in *Proc. Opt. Fiber Commun. Conf. Exhib.*, 2015, pp. 1–3.

[30] C. G. Askins, G. A. Miller, and E. J. Friebele, "Bend and twist sensing in a multiple-core optical fiber," in *Proc. Opt. Fiber Commun. Conf./Nat. Fiber Opt. Eng. Conf.*, 2008, Art. no. OMT3.

[31] R. Veronese *et al.*, "Experimental characterization of group and phase delays induced by bending and twisting in multi-core fibers," *Opt. Lett.*, vol. 46, no. 11, pp. 2674–2677, 2021.